Gallant: Voxel Grid-based Humanoid Locomotion and Local-navigation across 3D Constrained Terrains

Qingwei Ben[*,2,1], Botian Xu[*,2], Kailin Li[*,1], Feiyu Jia[1,3],
Wentao Zhang[4,1], Jingping Wang[1,5], Jingbo Wang[1], Dahua Lin[2,1], Jiangmiao Pang[⊕,1]

[1]Shanghai Artificial Intelligence Laboratory, [2]The Chinese University of Hong Kong,
[3]University of Science and Technology of China , [4]Tykyo University, [5]Shanghai Jiaotong University

[*]Equal Contribution, [⊕]Corresponding Author

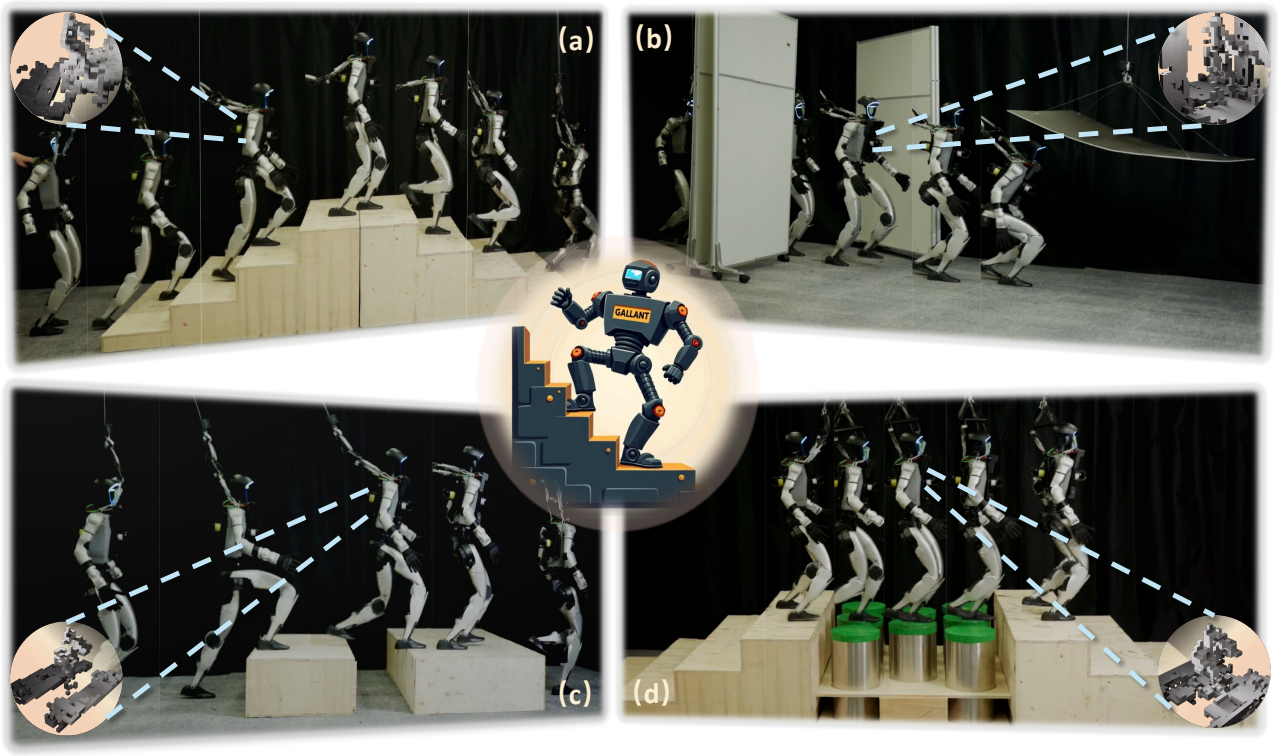

Figure 1. **Overview.** Gallant enables a single policy with voxel grids to traverse diverse 3D constrained terrains: (a) ascend and descend stairs, (b) pass doors and duck under ceilings, (c) step onto platforms and over gaps, and (d) cross stepping-stone pillars.

Abstract

Robust humanoid locomotion requires accurate and globally consistent perception of the surrounding 3D environment. However, existing perception modules, mainly based on depth images or elevation maps, offer only partial and locally flattened views of the environment, failing to capture the full 3D structure. This paper presents ***Gallant****, a voxel-grid–based framework for humanoid locomotion and local navigation in 3D constrained terrains. It leverages voxelized LiDAR data as a lightweight and structured perceptual representation, and employs a z-grouped 2D CNN to map this representation to the control policy, enabling fully end-to-end optimization. A high-fidelity LiDAR simulation that dynamically generates realistic observations is developed to support scalable, LiDAR-based training and ensure sim-to-real consistency. Experimental results show that Gallant's broader perceptual coverage facilitates the use of a single policy that goes beyond the limitations of previous methods confined to ground-level obstacles, extending to lateral clutter, overhead constraints, multi-level structures, and narrow passages. Gallant also firstly achieves near-100% success rates in challenging scenarios such as stair climbing and stepping onto elevated platforms through improved end-to-end optimization. Website: Gallant.*

1. Introduction

Robust humanoid locomotion in unstructured 3D environments demands accurate and globally consistent perception of surrounding geometry. While recent systems have progressed from lab prototypes to real-world deployment [17, 23, 36], ensuring operational safety remains a key challenge. Robots must not only traverse level surfaces, but also navigate terrain irregularities, ground-level obstacles, lateral clutter, and overhead constraints. This requires a perception architecture that enables anticipatory collision checking, clearance-aware motion generation, and planning of contact-rich maneuvers.

Existing perception modules, such as those based on depth images or elevation maps, provide only partial and locally flattened views of the environment, limiting the robot's understanding of complex 3D structures. Depth cameras[34, 49] offer lower-latency perception; however, their narrow field of view (FoV) and limited range impede reasoning about complex, spatially extended environments. In contrast, 3D LiDAR provides detailed scene geometry with a wide FoV, but its raw point clouds are sparse and noisy, which bottlenecks sample-efficient policy learning and real-time inference. Elevation-mapping approaches compress full 3D LiDAR point clouds into 2.5D height fields[2, 13, 21, 30, 38], yielding a bird's-eye height estimate for each ground-plane cell [10, 11]. This projection discards vertical and multilayer structure (e.g., overhangs, low ceilings, mezzanines, stair undersides), and the reconstruction stage can introduce algorithm-specific distortions and latency, further decoupling perception from control.

To address these limitations, we introduce **Gallant**, a voxel-**g**rid–based perception-learning framework for hum**a**noid **l**ocomotion and **l**oco-navigation **a**cross 3D co**n**strained **t**errains. Gallant uses a robot-centric voxel grid derived from LiDAR point clouds as its perception representation, preserving multi-layer scene structure over a large FoV while aggregating raw points into voxels to reduce dimensionality and smooth noise, yielding a lightweight tensor amenable to efficient learning. A *z-grouped* 2D convolutional neural network (CNN) treats height slices as channels, exploiting sparsity to produce compact features with a favorable accuracy–compute trade-off compared to heavier 3D CNNs [12, 25, 37]. These features are fused with proprioceptive signals and passed to a multi-layer perceptron (MLP)-based actor for whole-body control, directly conditioning actions on 3D structural cues. To scale training and narrow the simulation-to-reality (sim-to-real) gap, we develop a LiDAR simulation pipeline that models sensor noise and latency and enables realistic scanning of dynamic objects, including the robot's own moving links, thereby aligning synthetic data with deployment conditions. We further construct eight representative terrain families spanning ground-level obstacles, lateral clutter, and overhead constraints, encouraging the policy to internalize structural regularities critical for generalization.

Experimental results show that Gallant enables a single end-to-end policy that generalizes from simulation to diverse real-world environments, handling not only ground-level obstacles but also lateral clutter and overhead constraints—capabilities that were previously beyond the reach of existing methods. Gallant achieves near-100% success in challenging tasks such as stair climbing and platform stepping, while significantly improving robustness over elevation-based baselines. Experiments also highlight the importance of our high-fidelity LiDAR simulation, which dynamically generates realistic observations essential for scalable, LiDAR-based training. Ablation results further demonstrate the efficiency of the z-grouped 2D CNN, which attains superior performance and lower inference latency compared to 3D CNNs, making it well-suited for real-time humanoid deployment. These results establish Gallant as a practical, full-stack solution—from realistic LiDAR simulation to robust control—for full-space perceptive locomotion and local-navigation in 3D constrained environments. Our contribution lies in the following aspects:

1. We propose voxel grid as a lightweight yet geometry-preserving representation for humanoid locomotion and loco-navigation [31] in 3D-constrained environments.
2. We verify that z-grouped 2D CNN effectively processes voxel grids, offering a favorable trade-off between representation capacity and computational efficiency.
3. We develop a full-stack pipeline from sensor simulation to policy training, achieving a single policy that generalizes across diverse 3D-constrained terrains in real.

2. Related Work

Table 1. Comparison between gallant and previous methods. FoV in *Solid Angles* are computed by parameter of the used sensors.

Method	Perceptual Representation	Fov	Ground	Lateral	Overheading
Long et al. [21]	Elevation Map	$\sim 1.97\pi$	✓	✗	✗
Wang et al. [38]	Elevation Map	$\sim 1.97\pi$	✓	✗	✗
Ren et al. [30]	Elevation Map	$\sim 1.97\pi$	✓	✓	✗
Zhuang et al. [49]	Depth Image	$\sim 0.43\pi$	✓	✗	✗
Wang et al. [39]	Point Cloud	$\sim 1.97\pi$	✗	✓	✓
Gallant (ours)	Voxel Grid	$\sim 4.00\pi$	✓	✓	✓

Humanoid Perceptive Locomotion. Humanoid perceptive locomotion uses onboard sensing to traverse constrained terrains. Prior work mainly relies on elevation maps [21, 26, 30, 35, 38], trained with ground-truth height fields and deployed via LiDAR reconstruction [10, 11]. While effective for ground-level reasoning, elevation maps flatten the scene and ignore lateral or overhead structures,

and introduce reconstruction latency. Alternatively, depth cameras offer higher update rates and are proved to be effective on quadruped robots [1, 7, 18, 22, 34, 48, 49], but their narrow field of view and limited spatial continuity similarly restrict 3D understanding, hindering policy generalization in diverse environments. Recent LiDAR simulation advances enable realistic sensing during training. While point-cloud–based inputs [15, 39] address prior limitations, their high processing cost makes real-time onboard use infeasible. Voxel grids offer a structured, efficient alternative [12, 27]. They have been explored for cross-modal perception for scene-understanding on legged robots [9, 33, 47], but remain unused in humanoid locomotion as a direct way of perception. To this end, Gallant introduces a LiDAR perception framework tailored for scalable simulation and real-time deployment, using voxel grids to support a single policy capable of zero-shot sim-to-real transfer and full 3D obstacle handling. A comparison of Gallant with prior methods in perceptual representation, FoV, and supported obstacle types is listed in Tab. 1.

Local Navigation. Local navigation enables legged robots to reach targets in cluttered, constrained environments while minimizing incidental contact. Most systems adopt a hierarchical design: a high-level planner outputs velocity commands, and a low-level policy tracks them [4, 6, 12, 15, 20, 29, 40, 45, 46]. This decoupling limits the policy's ability to exploit terrain, and tracking errors—combined with slow high-level updates, further degrading performance. Recent work explores end-to-end training by adding obstacle-avoidance rewards to velocity tracking [30], but this creates conflicting objectives. Using target positions instead allows the policy to reason over terrain and choose appropriate actions [14, 31, 44], though this remains untested on humanoids. Gallant adopts this position-based formulation to fuse local navigation and locomotion into one single policy.

3. Method

We introduce **Gallant**, a voxel-grid–based perceptive learning framework for humanoid locomotion and local navigation [31] in 3D constrained environments. As shown in Fig. 2, the system comprises: (i) a parallelized LiDAR simulation pipeline (Sec. 3.2), (ii) a lightweight 2D CNN perception module tailored to sparse voxel grids (Sec. 3.3), and (iii) a set of representative terrain families for curriculum training (Sec. 4.1). Together, these components form a full-stack pipeline—from data generation to perception to control—that trains a single policy to robustly traverse all-space obstacles and deploy zero-shot on real hardware.

3.1. Problem Formulation

We formulate humanoid perceptive locomotion as a partially observable Markov decision process (POMDP) $\mathcal{M} = (\mathcal{S}, \mathcal{A}, \mathcal{O}, P, \mathcal{R}, \Omega, \gamma)$ and train an actor–critic policy using Proximal Policy Optimization (PPO) [32]. The training environment is divided into $8\,\mathrm{m} \times 8\,\mathrm{m}$ blocks. At each episode, the humanoid starts at the block center, and a goal $\mathbf{G}$ is sampled along the perimeter, with a fixed horizon of 10 seconds for robots to reach. The observation at time t is defined as:

$$o_t = (\underbrace{\mathbf{P}_t,\, \mathbf{T}_{\text{elapse},t},\, \mathbf{T}_{\text{left},t}}_{\text{Command}},\ \underbrace{a_{t-4:t-1}}_{\text{Action history}},$$
$$\underbrace{\omega_{t-5:t},\, g_{t-5:t},\, q_{t-5:t},\, \dot{q}_{t-5:t}}_{\text{Proprioception}},$$
$$\underbrace{\texttt{Voxel\_Grid}_t}_{\text{Perception}},\ \underbrace{v_t,\, \texttt{Height\_Map}_t}_{\text{Privileged}}),$$

where: $\mathbf{P}_t$ is the goal position relative to the robot base, $\mathbf{T}_{\text{elapse},t}$ is the elapsed time in the episode, $\mathbf{T}_{\text{left},t} = T - \mathbf{T}_{\text{pass},t}$ is the remaining time until timeout ($T = 10$s), a_t denotes actions output by policy, ω_t and v_t are the root angular and linear velocity of the robot, g_t is the vector $[0, 0, -1]$ projected into the robot base frame, q_t and $\dot{q}_t$ are joint positions and velocities, respectively, $\texttt{Voxel\_Grid}_t$ is the voxelized perception input, $\texttt{Height\_Map}_t$ is relative heights of the scanned dots to the robot. Here, the subscript range $t-a : t-b$ denotes inclusion of temporal history from time step $t-a$ to $t-b$. Actor and critic share all features except privileged inputs, which are critic-only. The reward follows Ben et al. [3] with velocity tracking rewards replaced by goal-reaching reward [31]:

$$r_{\text{reach}} = \frac{1}{1 + \|\mathbf{P}_t\|^2} \cdot \frac{\mathbb{1}(t > T - T_r)}{T_r} \ (T_r = 2s),$$

allowing time for trajectory exploration. The objective is to maximize expected return $J(\pi) = \mathbb{E}[\sum_{t=0}^{H-1} \gamma^t r_t]$. Episodes end on fall, harsh collision, or timeout. Network and reward details are listed in Appendix.

3.2. Efficient LiDAR Simulation

Most GPU-based simulators, such as IsaacGym and IsaacSim, either lack native support for efficient LiDAR simulation or are limited to scanning a single static mesh. However, realistic simulation in dynamic environments requires accounting for all relevant geometry, including both static and dynamic meshes—especially bodies of robots. To address this, we implement a lightweight, efficient raycast-voxelization pipeline using NVIDIA Warp [24]. Traditional raycasting builds a Bounding Volume Hierarchy (BVH) over scene geometry, which becomes costly if updated at every simulation step due to dynamics. To mitigate this, we precompute a BVH for each mesh in its local (body) frame. During simulation, the ray origin $\mathbf{p}$ is transformed, and only the rotation component is applied to the direction $\mathbf{d}$, rotating the ray into the mesh's local frame. To be specific, the

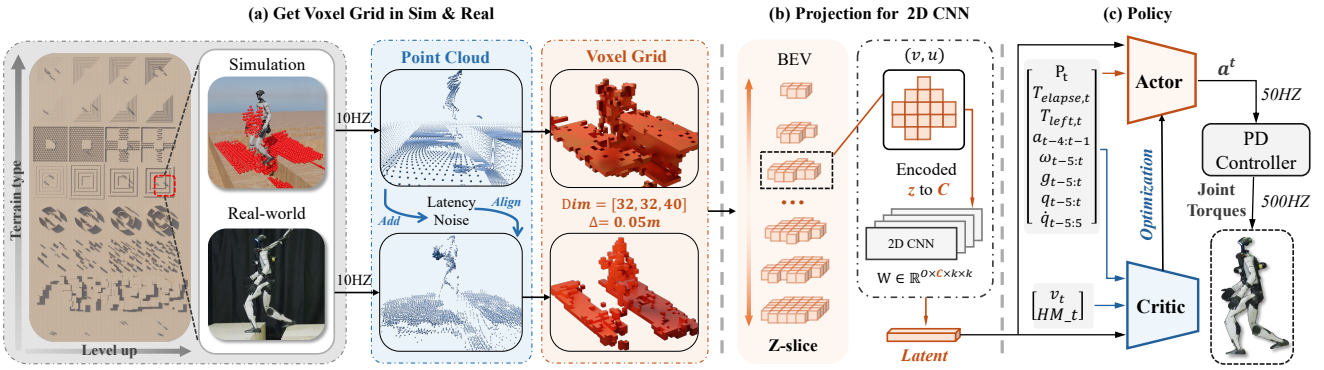

Figure 2. **Method Overview.** (a) Curriculum-based training over 8 representative terrains enhances generalization. (b) Realistic voxel path alignment achieved via efficient LiDAR simulation with domain-randomized latency and noise. (c) A 2D CNN-based perceptual module processes voxel grid using the z-dimension as input channels, balancing efficiency and representation capability. (d) A latent-aware PPO policy enables zero-shot sim-to-real transfer across diverse obstacles, including ground, lateral, and overhead challenges.

raycasting is performed as:

$$\text{raycast}(TM, \mathbf{p}, \mathbf{d}) = T^{-1}\text{raycast}(M, T^{-1}\mathbf{p}, R^{-1}\mathbf{d}),$$

Here, T denotes the full transformation matrix, and R its rotational component. The function returns the ray–mesh intersection point. At each simulation step, ray–mesh intersections are computed for every mesh M using its transform T_t, parallelized via a Warp kernel of shape $(N_{\text{envs}}, N_{\text{meshes}}, N_{\text{rays}})$. Rays are emitted from the LiDAR origin P_{LiDAR} in directions defined as $O_{\text{ray}_i} = O_{\text{LiDAR}} + O_{\text{ray}_i,\text{offset}}$, where $O_{\text{ray}_i,\text{offset}}$ is the i-th ray's direction offset from the LiDAR orientation. Let P_i be the hit position of the i-th ray; the resulting point cloud is: $\mathcal{P}_t = \bigcup_{i=1}^{N_{\text{rays}}} \{P_i\}$, which is subsequently used to construct the voxel grid. To align simulation with real-world sensing, we apply domain randomization: *(a) LiDAR Pose:* Perturbed at episode start by $P^{\text{rand}}_{\text{LiDAR}} = P_{\text{LiDAR}} + \mathcal{N}(0, 1)$ (cm) and $O^{\text{rand}}_{\text{ray}_i} = O_{\text{LiDAR}} + \mathcal{N}(0, (\frac{\pi}{180})^2) + O_{\text{ray}_i,\text{offset}}$ (rad); *(b) Hit Position:* $P^{\text{rand}}_i = P_i + \mathcal{N}(0, 1)$ (cm); *(c) Latency:* Simulated at 10 Hz with 100–200 ms delay; *(d) Missing Grid:* Randomly mask 2% of voxels to model real-world dropout. These augmentations reduce the sim-to-real gap and improve policy transferability.

3.3. Voxel Representation and 2D CNN Perception

We convert LiDAR point clouds into a fixed-size, robot-centric voxel grid. At each timestep, returns from two torso-mounted LiDARs are transformed into a unified torso frame. The perception volume is defined as a cuboid $\Omega = [-0.8, 0.8]\,\text{m} \times [-0.8, 0.8]\,\text{m} \times [-1.0, 1.0]\,\text{m}$, discretized at resolution $\Delta = 0.05\,\text{m}$, yielding a $32 \times 32 \times 40$ grid along the x, y, and z axes respectively. Each voxel is set to 1 if at least one LiDAR point lies inside its volume, and 0 otherwise, producing a binary occupancy tensor $X \in \{0, 1\}^{C\times H\times W}$, where $C = 40$ (height slices), $H = W = 32$ (spatial resolution).

Due to the line-of-sight nature of LiDAR and the structured nature of typical terrains, the voxel grid is highly sparse and locally concentrated: most (x, y) columns contain only one or two occupied z-slices, and large contiguous spatial regions may remain completely empty. Rather than applying computationally expensive 3D convolutions over the full volume, we treat the z-axis as the channel dimension and apply 2D convolutions over the $x - y$ plane. This leverages spatial context while using channel mixing to capture vertical structure, making effective use of the sparse, localized occupancy pattern. Formally, let $X \in \mathbb{R}^{C\times H\times W}$ be the voxel input and $\mathbf{W} \in \mathbb{R}^{O\times C\times k\times k}$ the weights of a 2D convolution. The output $Y \in \mathbb{R}^{O\times H\times W}$ is computed:

$$Y_{o,v,u} = \sigma\left(\sum_{c=0}^{C-1}\sum_{\Delta v,\Delta u} \mathbf{W}_{o,c,\Delta v,\Delta u} \cdot X_{c,v+\Delta v,u+\Delta u} + b_o\right),$$

where σ is a nonlinearity and b_o is a bias term. Compared to a 3D kernel of size k^3, this design reduces compute and memory cost by roughly a factor of k, while still capturing the vertical patterns critical for locomotion. Moreover, the 2D structure enables efficient parallel training and supports real-time inference on onboard compute.

3.4. Terrain Design

We design 8 representative terrain types to train robots in simulation: **Plane** represents the easiest terrain and helps robots learn to walk in the early stage; **Ceiling** with randomized height and density requires reasoning about overhead constraints and crouching; **Forest**, composed of randomly spaced cylindrical pillars, represents sparse lateral clutter requiring weaving behavior; **Door** presents narrow gaps demanding precise lateral clearance; **Platform** consists of high, ring-shaped structures with variable spacing and height, requiring recognition of stepable surfaces and inter-platform traversal; **Pile** introduces fine-grained sup-

Table 2. Parameters for generating curriculum training terrains.

Terrain Type τ	Term	$\mathbf{p}_\tau^{\min}$	$\mathbf{p}_\tau^{\max}$
Ceiling	Ceiling height $(m)\downarrow$	1.30	1.00
	Number of Ceiling (-) $\uparrow$	10	40
Forest	Minimum distance between trees $(m)\downarrow$	2.0	1.0
	Number of trees (-) $\uparrow$	3	32
Door	Distance between two walls $(m)\downarrow$	2.00	1.00
	Width of the doors $(m)\downarrow$	1.60	0.80
Platform	Height of the platforms $(m)\uparrow$	0.05	0.35
	Gap width between two platforms $(m)\uparrow$	0.20	0.50
Pile	Distance between two cylinders $(m)\uparrow$	0.35	0.45
Upstair	Height of each step $(m)\uparrow$	0.00	0.20
	Width of each step $(m)\downarrow$	0.50	0.30
Downstair	Height of each step $(m)\uparrow$	0.00	0.20
	Width of each step $(m)\downarrow$	0.50	0.30

port reasoning for safe foot placement; **Upstair** and **Downstair** require continuous adaptation to vertical elevation.

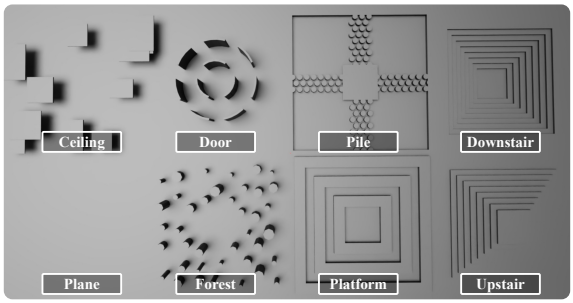

Figure 3. Terrain types used to train robots in simulation($\mathbf{p}_\tau^{\max}$)

We adopt a curriculum-based training strategy where terrain difficulty increases progressively. Each terrain type τ is parameterized by a scalar difficulty $s \in [0, 1]$. Terrain generation parameters are interpolated as:

$$\mathbf{p}_\tau(s) = (1 - s)\,\mathbf{p}_\tau^{\min} + s\,\mathbf{p}_\tau^{\max},$$

where $\mathbf{p}_\tau^{\min}$ and $\mathbf{p}_\tau^{\max}$ denote the easiest and hardest settings (see Tab. 2). In each episode, a 10s goal-reaching task is assigned, and success results in promotion to harder settings; failure leads to demotion. To support learning on **Pile**, we overlay a flat surface during early training (low s), following [38], allowing the robot to first learn basic foothold placement. For high s, the plane is removed, and training continues on fully gapped terrain for true crossing behavior.

4. Experiments

4.1. Experimental Configuration

We conduct both simulation training and real-world deployment on the 29-DoF Unitree G1 humanoid. Simulation is performed using NVIDIA IsaacSim [28]. To ensure voxel grids accurately capture full-space terrain geometry, we mount two Hesai JT128 LiDARs on the robot—one on the front chest and one on the back—each with a $95° \times 360°$ field of view. This dual-sensor configuration is identically replicated in simulation to ensure consistent perception across domains. Policy training is distributed across eight NVIDIA RTX 4090 GPUs (45GB memory each). During deployment, both the learned policy and voxel grid processing run entirely onboard the G1 using an NVIDIA Orin NX. For target-relative localization, we use a Livox Mid-360 LiDAR mounted on the robot's head and process its data using FastLIO2 [42, 43]. This LiDAR also provides input for elevation map generation in baseline comparisons.

4.2. Simulation Experiments

4.2.1. Metrics

We evaluate ablated methods in IsaacSim [28] on the most challenging terrain settings ($\mathbf{p}_\tau^{\max}$; Sec. 4.1), and the policy performance is measured by two distinct metrics:

- **Success rate** E_{succ}: fraction of episodes that reach the target within a 10s horizon without falling or incurring any severe collisions with the obstacles.
- **Collision momentum** $E_{\text{collision}}$: cumulative momentum transferred through unnecessary contacts (all robot–environment contacts excluding nominal foot contacts), reflecting the policy's ability to avoid collisions.

We train every policy for $4{,}000$ iterations, then run 5 independent evaluations (each run evaluates over $1{,}000$ complete episodes), reporting mean $\pm$ standard deviation; policies with higher E_{succ} and lower E_{col} are better.

4.2.2. Baselines

To assess the effectiveness of core components in Gallant, we compare against the following ablations:

- **Self-scan.** We disable simulated LiDAR returns from dynamic geometry (e.g. the robot's own links), but only scans static terrain. This is compared to **Gallant**, which models scans over both static terrain and moving links.
- **Perceptual network.** We replace the z-as-channel 2D CNN with alternatives: standard 3D CNN, sparse 2D CNN, and sparse 3D CNN (commonly used in LiDAR perception [5, 12]). Sparse variants are based on [8].
- **Perceptual representation.** Gallant feeds a voxel grid to the actor and a voxel grid plus a height map to the critic. We test two baselines to isolate this: (i) only height map for actor and critic; (ii) only voxel grid for actor and critic.
- **Voxel resolution.** We sweep the voxel size around the default 5 cm (i.e., 2.5 cm and 10 cm) to examine the trade-off between field of view coverage and geometric fidelity.

4.2.3. Result

Across eight representative terrains, Gallant attains superior success rates relative to the baselines (see Tab. 3). Ablation-specific analyses are summarized as follow:

LiDAR return from dynamic objects is necessary. With all other settings fixed, Gallant achieves much higher

Table 3. **Simulation ablation results.** We present a success rate comparison between **Gallant** and baselines on the eight representative terrains. The means and standard variation are reported across 5 evaluations, each with 1,000 testing episodes. Success rate is reported as a percentage (e.g., 90 means 90%). For each ablation setting, the best-performing value per metric on each terrain is highlighted in bold.

Method	Plane		Ceiling		Forest		Door		Platform		Pile		Upstair		Downstair	
	$E_{\text{succ}}\uparrow$	$E_{\text{collision}}\downarrow$	$E_{\text{succ}}\uparrow$	$E_{\text{collision}}\downarrow$	$E_{\text{succ}}\uparrow$	$E_{\text{collision}}\downarrow$	$E_{\text{succ}}\uparrow$	$E_{\text{collision}}\downarrow$	$E_{\text{succ}}\uparrow$	$E_{\text{collision}}\downarrow$	$E_{\text{succ}}\uparrow$	$E_{\text{collision}}\downarrow$	$E_{\text{succ}}\uparrow$	$E_{\text{collision}}\downarrow$	$E_{\text{succ}}\uparrow$	$E_{\text{collision}}\downarrow$
(a) Ablation on Self-scan																
w/o-Self-Scan	99.7 (±0.1)	1.6 (±3.2)	28.4 (±2.4)	442.7 (±22.1)	78.1 (±1.4)	420.5 (±12.1)	98.3 (±0.7)	152.7 (±20.0)	22.16 (±1.2)	637.6 (±31.3)	27.2 (±1.0)	579.0 (±55.1)	33.0 (±0.9)	305.5 (±16.6)	96.6 (±0.4)	15.15 (±6.1)
Gallant	**100.0** (±0.0)	**0.0** (±0.0)	**97.1** (±0.6)	**24.6** (±6.3)	**84.3** (±0.7)	**311.1** (±25.9)	**98.7** (±0.3)	**27.7** (±6.4)	**96.1** (±0.5)	**30.1** (±5.3)	**82.1** (±0.6)	**113.1** (±14.6)	**96.2** (±0.6)	**27.0** (±4.9)	**97.9** (±0.4)	**15.6** (±6.2)
(b) Ablation on Perceptual Network																
Sparse-3D-CNN	100.0 (±0.0)	0.0 (±0.0)	86.7 (±2.0)	143.5 (±46.1)	84.1 (±1.5)	**277.8** (±22.1)	98.0 (±.06)	74.8 (±7.9)	88.8 (±1.5)	96.8 (±11.6)	52.4 (±1.5)	365.9 (±12.3)	80.1 (±2.2)	107.7 (±15.8)	97.5 (±0.4)	18.9 (±14.1)
3D-CNN	99.9 (±0.1)	0.0 (±0.0)	**97.5** (±0.5)	**20.0** (±6.6)	73.9 (±2.1)	379.0 (±70.2)	96.1 (±0.7)	69.58 (±5.8)	92.7 (±1.0)	65.6 (±9.5)	65.3 (±0.9)	275.4 (±31.5)	86.0 (±1.4)	78.1 (±19.2)	**99.0** (±0.3)	12.1 (±11.6)
Sparse-2D-CNN	99.6 (±0.2)	0.7 (±1.4)	96.0 (±1.0)	26.17 (±5.1)	80.2 (±1.1)	363.1 (±14.4)	92.7 (±1.0)	199.6 (±120.2)	87.9 (±1.1)	100.5 (±20.3)	57.6 (±0.9)	360.3 (±16.3)	89.1 (±0.7)	52.9 (±4.8)	98.7 (±0.6)	**4.55** (±2.92)
Gallant	**100.0** (±0.0)	**0.0** (±0.0)	97.1 (±0.6)	24.6 (±6.3)	**84.3** (±0.7)	311.1 (±25.9)	**98.7** (±0.3)	**27.7** (±6.4)	**96.1** (±0.5)	**30.1** (±5.3)	**82.1** (±0.6)	**113.1** (±14.6)	**96.2** (±0.6)	**27.0** (±4.9)	97.9 (±0.4)	15.6 (±6.2)
(c) Ablation on Perceptual Interface																
Only-Height-Map	100.0 (±0.0)	0.0 (±0.0)	5.3 (±2.0)	1995.3 (±68.3)	10.5 (±1.5)	577.4 (±18.1)	10.2 (±1.3)	717.5 (±33.8)	96.0 (±0.7)	34.3 (±2.8)	**86.2** (±0.6)	**101.6** (±13.8)	**98.3** (±0.2)	**11.6** (±6.2)	98.5 (±0.3)	11.2 (±6.7)
Only-Voxel-Grid	100.0 (±0.0)	0.0 (±0.0)	96.9 (±0.4)	**22.4** (±4.2)	75.9 (±1.5)	506.0 (±20.6)	96.0 (±0.3)	281.4 (±29.0)	94.2 (±0.8)	51.0 (±10.2)	72.3 (±0.6)	201.8 (±14.9)	89.3 (±1.3)	46.9 (±10.5)	**98.8** (±0.2)	**7.0** (±3.9)
Gallant	**100.0** (±0.0)	**0.0** (±0.0)	**97.1** (±0.6)	24.6 (±6.3)	**84.3** (±0.7)	**311.1** (±25.9)	**98.7** (±0.3)	**27.7** (±6.4)	**96.1** (±0.5)	**30.1** (±5.3)	82.1 (±0.6)	113.1 (±14.6)	96.2 (±0.6)	27.0 (±4.9)	97.9 (±0.4)	15.6 (±6.2)
(d) Ablation on Voxel Resolution																
10CM	98.8 (±0.2)	2.1 (±1.6)	**97.3** (±0.9)	**24.2** (±11.0)	77.5 (±3.4)	368.0 (±36.3)	97.5 (±0.4)	260.4 (±38.8)	75.5 (±0.5)	63.0 (±4.9)	65.2 (±5.5)	256.3 (±50.0)	94.1 (±1.1)	38.6 (±6.7)	97.5 (±0.4)	**13.5** (±2.0)
2.5CM	99.9 (±0.1)	2.1 (±1.6)	13.3 (±2.4)	1442.4 (±119.6)	59.0 (±1.7)	642.7 (±12.4)	64.8 (±1.1)	591.0 (±22.5)	67.2 (±2.7)	268.9 (±39.3)	54.1 (±1.7)	400.2 (±19.5)	86.3 (±1.2)	74.8 (±12.8)	96.6 (±0.4)	15.2 (±6.1)
Gallant (5CM)	**100.0** (±0.0)	**0.0** (±0.0)	97.1 (±0.6)	24.6 (±6.3)	**84.3** (±0.7)	**311.1** (±25.9)	**98.7** (±0.3)	**27.7** (±6.4)	**96.1** (±0.5)	**30.1** (±5.3)	**82.1** (±0.6)	**113.1** (±14.6)	**96.2** (±0.6)	**27.0** (±4.9)	**97.9** (±0.4)	15.6 (±6.2)

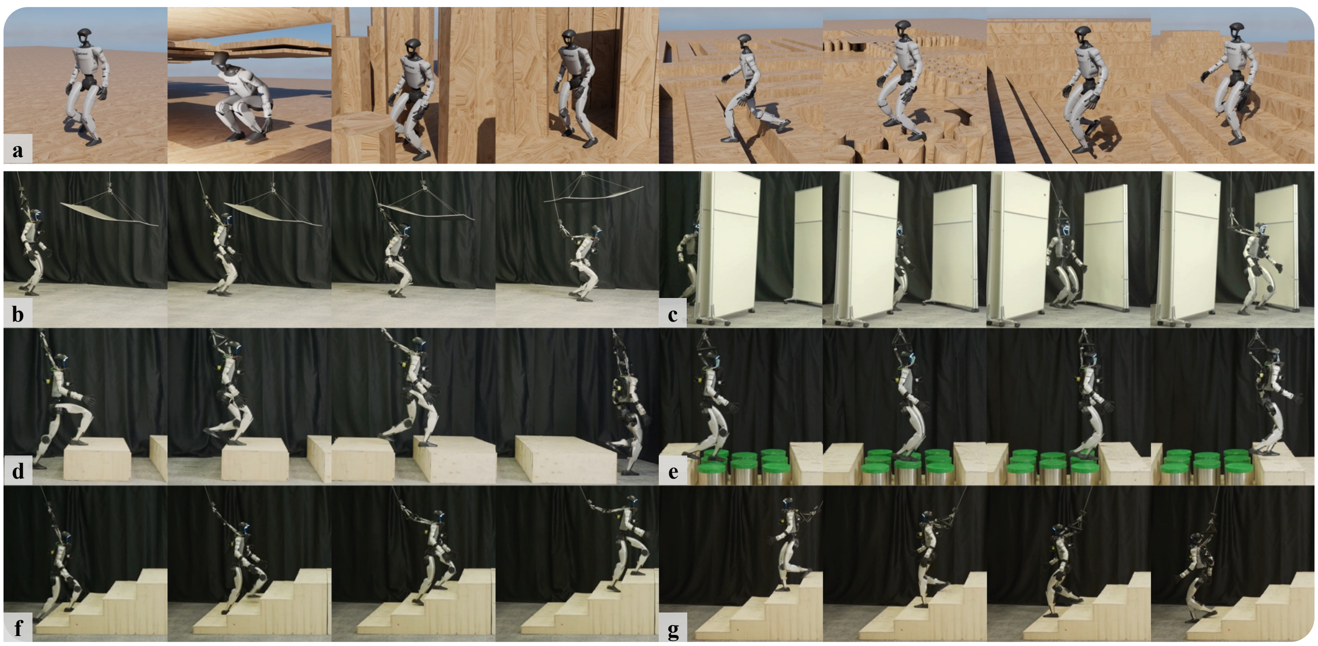

Figure 4. Humanoid robot traverses diverse 3D constrained terrains in both simulation and the real world. (a)Traversal across the eight simulated training terrain types. (b)Ducking under suspended ceiling obstacles. (c)Local navigation through lateral clutters. (d)Stepping onto a $30cm$-high platform and crossing a $40cm$ gap. (e)Traversing pile-like stepping-stone terrain. (f)(g)Ascending and descending $20cm$ stairs. All deployments are based on the **same policy**.

success rates than the variant that ignores dynamic objects (w/o-Self-Scan) across all tasks. Using Ceiling as an example in Fig. 5 (a), when the robot ducks under the ceiling, the voxel grids with dynamics (Fig. 5 (b)) correctly include the robot's legs, which occupy voxels and induce occlusion "holes" along LiDAR rays to the distant floor. In contrast, excluding dynamics (Fig. 5 (c)) yields an artificially flat floor. Because real LiDAR returns from all visible objects, omitting dynamics makes the voxel grid out-of-distribution (OOD) in postures where the body is not fully upright (e.g., Ceiling, Platform), causing a pronounced drop in success. Hence, simulating dynamic objects in the LiDAR pipeline is critical to final performance. **z-grouped 2D CNN is the most suitable choice.** Although one variant marginally exceeds Gallant on a few terrains (e.g., a 3D CNN on Ceiling), the gains are small and are outweighed by lower success rates on most tasks. Our voxel input is a compact, egocentric grid of $32\times32\times40$, which changes with the torso frame. As shown in Fig. 5 (d), sparse convolutions offer little advantage: occupancy is relatively dense in the $x-y$ plane, so few computations are actually skipped, while the rule-book overhead of sparse kernels becomes a dominant cost

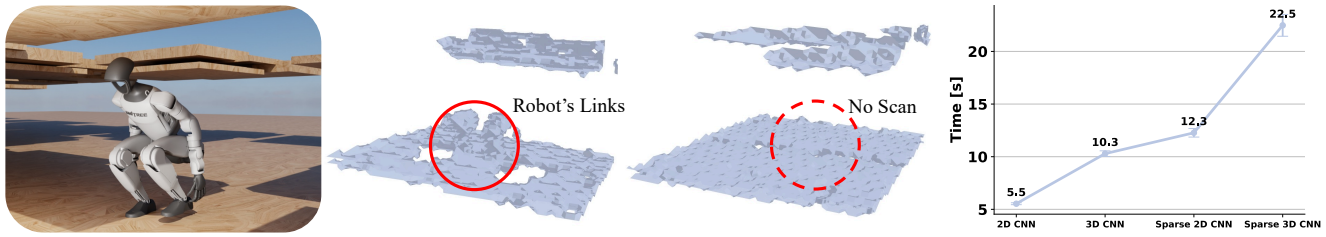

(a)Humanoid Crossing Ceiling (b)Voxel Grid w/ Self-scan (c)Voxel Grid w/o Self-scan (d) Mean Training Iteration Time

Figure 5. **Visualization of simulation ablation analyses.** (a) The humanoid crouches to traverse under a low ceiling; (b) Voxel grid from LiDAR simulation that includes dynamic objects captures the robot's own links; (c) LiDAR simulation restricted to static objects excludes robot links from the voxel grid; (d) Mean training iteration time for Gallant with different CNN-based perception modules.

at this scale. On the other hand, full 3D CNNs introduce substantially more parameters and memory traffic, making optimization harder and less data-efficient when sparsity is concentrated primarily along z. Treating z as channels with a lightweight 2D CNN preserves vertical structure through channel mixing, exploits highly optimized dense 2D operators, and provides the right inductive bias for an egocentric raster that is approximately translation-equivariant in $x-y$ yet rotates with the body. In practice, this z-grouped 2D design delivers equal or better accuracy with markedly lower compute, making it the most suitable choice for our task.

Combination of Voxel Grid and Height Map is better. As discussed in Sec. 1, using only a height map as the perceptual representation for policy cannot represent multi-layer structure; consequently, Only-Height-Map fails on terrains such as Ceiling. Nevertheless, in simulation (where the height map incurs no latency), height-map–based methods perform strongly on ground obstacles, indicating that the height map provides a useful, positively informative signal for training. For sim-to-real robustness, Gallant therefore omits the height map from the actor inputs, but includes it as part of the critic observation (privileged information). This asymmetric design leverages the height map to shape values and improve credit assignment during training while keeping the deployed policy free of latency-sensitive channels. This Gallant configuration achieves higher success rates than Only-Voxel-Grid (critic without height map) across all tasks, validating the proposed design.

5cm is a suitable resolution for Gallant. PPO training benefits from large batches collected over many parallel environments. Under a fixed VRAM budget, we therefore adjust the voxel-grid resolution to trade spatial precision for egocentric FoV. Empirically, the $10\,\mathrm{cm}$ grid underperforms Gallant's $5\,\mathrm{cm}$ setting: while it enlarges the FOV, its coarse quantization impairs fine contact- and clearance-sensitive interactions. Conversely, the $2.5\,\mathrm{cm}$ grid yields an even lower success rate: despite its higher precision, the reduced FOV hampers perception of long vertical extents, making terrains that require sensing far below or above the robot (e.g., Ceiling, Downstair) notably harder. Overall, the $5\,\mathrm{cm}$ resolution strikes an effective balance between coverage and detail under resource constraints.

4.3. Real-world Experiments

4.3.1. Deployment

We directly deploy the Gallant-trained policy onto the real Unitree G1 humanoid without any fine-tuning. The control loop runs at $50Hz$, consistent with simulation. To ensure reliable voxel input, raw point clouds from dual LiDARs are processed onboard using OctoMap [16], generating a binary occupancy grid at $10Hz$. Importantly, OctoMap serves as a lightweight preprocessing step—not a full reconstruction pipeline like elevation maps—and thus incurs minimal latency or computational load.

We evaluate the same policy across a variety of real-world scenarios, including flat terrain, random-height ceilings, lateral clutters (e.g., doors), high platforms with gaps, stepping stones, and staircases. Despite the diverse and complex constraints, the robot consistently traverses these terrains with high success rates (see Fig. 6). Qualitative results are shown in Fig. 4. The policy exhibits versatile capabilities: it crouches under ceilings of varying heights, plans lateral motions to pass through narrow doorways, steps robustly onto high platforms, crosses gaps between them, and carefully places its feet to negotiate stepping-stone–like terrains. On stairs, it demonstrates stable multi-step climbing and descent without loss of balance. These results highlight Gallant's ability to encode spatial constraints from perception and translate them into robust, real-time whole-body behaviors. Furthermore, all behaviors arise from a single policy without any terrain-specific tuning, highlighting Gallant's generality and real-world transferability.

4.3.2. Ablation

To evaluate sim-to-real performance, we deploy three policies on the 29-DoF Unitree G1 and compare success rates across terrains: (i) HeightMap, which replaces the voxel grid with an elevation map estimated from Livox Mid360; (ii) NoDR, trained without the LiDAR domain randomization described in Sec. 3.2, but otherwise identical to Gallant;

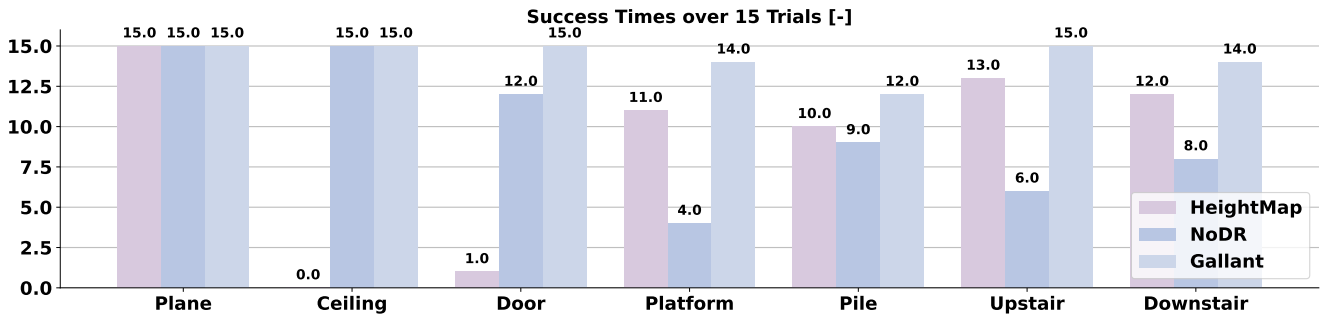

Figure 6. **Real-world traversal success times over 15 trials.** *Height Map* uses elevation maps as perceptual representation; *NoDR* is Gallant without LiDAR domain randomization; Gallant denotes the full proposed pipeline. All methods are tested for 15 trials per terrain.

and (iii) Gallant, our full pipeline. Each policy is tested over 15 trials per terrain, with results shown in Fig. 6.

Gallant consistently outperforms both baselines across all real-world terrains. The HeightMap baseline fails on overheading (e.g., Ceiling) and lateral (e.g., Door) obstacles due to its limited 2.5D representation, and performs worse than Gallant even on ground-level terrains. Unlike in simulation, where HeightMap occasionally excels on Pile or Stairs, its real-world performance is hindered by noisy elevation reconstruction. Moreover, our policy allows torso pitch/roll for more expressive motion, but this introduces LiDAR jitter at the mounting point, further degrading elevation map quality—reinforcing the benefit of voxel grids. The NoDR variant performs reasonably well on Ceiling and Door, suggesting low sensitivity to sensing latency in these cases. However, its performance drops significantly on ground-level terrains. Without modeling LiDAR delay and noise in training, the robot misjudges its position relative to obstacles, often reacting too late. This emphasizes the critical role of domain randomization in bridging the sim-to-real gap.

4.4. Further Analyses

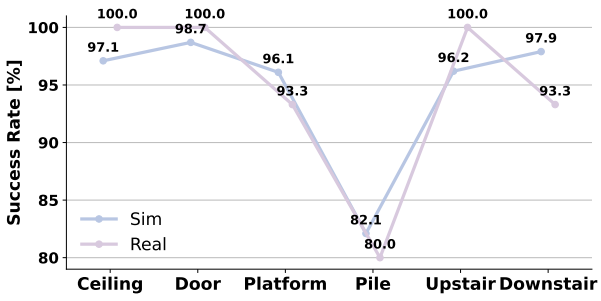

Figure 7. Gallant success rate in simulation and real world.

We analyze Gallant's success rates across terrains evaluated in both simulation and the real world (Fig. 7). A clear correlation emerges: terrains with higher success in simulation also perform well on hardware, validating the use of large-scale simulated evaluation as a reliable predictor of real-world performance. With the introduction of voxel grids, scenarios like overheading (e.g., Ceiling) and lateral (e.g., Door) constraints—previously difficult for height map-based methods—become the easiest considering the high success rate, demonstrating voxel grids as a simple yet effective representation for full-space perception.

Gallant's main limitation appears on the Pile terrain, where accurate foothold selection is critical. Success rates plateau around 80%, and simulation with zero LiDAR latency improves this to over 90%, indicating that real-world sensor delay is a key bottleneck. On other terrains—especially Platforms and Stairs, previously considered unstable due to collision risk [21]—Gallant achieves high success by proactively adjusting foot trajectories.

5. Conclusion

We present Gallant, a full-stack pipeline for humanoid locomotion and local navigation in 3D-constrained environments. It leverages voxel grids as a lightweight, geometry-preserving perceptual representation, combined with realistic LiDAR simulation and a z-grouped 2D CNN for efficient processing. Simulation ablations show that Gallant's key components are essential for training high–success-rate policies. In real-world tests, a single LiDAR policy covers the ground obstacles handled by elevation-map controllers while also tackling lateral and overhead structures, and on ground-only terrains it reaches near-100% success with fewer collisions. All these results together establish Gallant as a solid pipeline for humanoid locomotion and local navigation across 3D-constrained terrains.

Limitations. Despite its success, Gallant does not yet achieve a 100% success rate. The primary bottleneck lies in LiDAR latency: operating at 10 Hz, each scan incurs over 100 ms delay due to light reflection and communication overhead. This delay limits the robot's ability to act preemptively. Future work will explore using Gallant as a geometry-aware teacher while investigating lower-latency sensors to enable a fully reactive policy that achieves near-perfect performance across all terrains.

References

[1] Ananye Agarwal, Ashish Kumar, Jitendra Malik, and Deepak Pathak. Legged locomotion in challenging terrains using egocentric vision. In *Conference on robot learning*, pages 403–415. PMLR, 2023. 3

[2] Arthur Allshire, Hongsuk Choi, Junyi Zhang, David McAllister, Anthony Zhang, Chung Min Kim, Trevor Darrell, Pieter Abbeel, Jitendra Malik, and Angjoo Kanazawa. Visual imitation enables contextual humanoid control. *arXiv preprint arXiv:2505.03729*, 2025. 2

[3] Qingwei Ben, Feiyu Jia, Jia Zeng, Junting Dong, Dahua Lin, and Jiangmiao Pang. Homie: Humanoid loco-manipulation with isomorphic exoskeleton cockpit. *arXiv preprint arXiv:2502.13013*, 2025. 3, 2

[4] Wenzhe Cai, Jiaqi Peng, Yuqiang Yang, Yujian Zhang, Meng Wei, Hanqing Wang, Yilun Chen, Tai Wang, and Jiangmiao Pang. Navdp: Learning sim-to-real navigation diffusion policy with privileged information guidance. *arXiv preprint arXiv:2505.08712*, 2025. 3

[5] Yukang Chen, Jianhui Liu, Xiangyu Zhang, Xiaojuan Qi, and Jiaya Jia. Voxelnext: Fully sparse voxelnet for 3d object detection and tracking. In *Proceedings of the IEEE/CVF conference on computer vision and pattern recognition*, pages 21674–21683, 2023. 5

[6] An-Chieh Cheng, Yandong Ji, Zhaojing Yang, Zaitian Gongye, Xueyan Zou, Jan Kautz, Erdem Bıyık, Hongxu Yin, Sifei Liu, and Xiaolong Wang. Navila: Legged robot vision-language-action model for navigation. *arXiv preprint arXiv:2412.04453*, 2024. 3

[7] Xuxin Cheng, Kexin Shi, Ananye Agarwal, and Deepak Pathak. Extreme parkour with legged robots. In *2024 IEEE International Conference on Robotics and Automation (ICRA)*, pages 11443–11450. IEEE, 2024. 3

[8] Spconv Contributors. Spconv: Spatially sparse convolution library. https://github.com/traveller59/spconv, 2022. 5

[9] Wei Cui, Haoyu Wang, Wenkang Qin, Yijie Guo, Gang Han, Wen Zhao, Jiahang Cao, Zhang Zhang, Jiaru Zhong, Jingkai Sun, et al. Humanoid occupancy: Enabling a generalized multimodal occupancy perception system on humanoid robots. *arXiv preprint arXiv:2507.20217*, 2025. 3

[10] Péter Fankhauser, Michael Bloesch, Christian Gehring, Marco Hutter, and Roland Siegwart. Robot-centric elevation mapping with uncertainty estimates. In *International Conference on Climbing and Walking Robots (CLAWAR)*, 2014. 2

[11] Péter Fankhauser, Michael Bloesch, and Marco Hutter. Probabilistic terrain mapping for mobile robots with uncertain localization. *IEEE Robotics and Automation Letters (RA-L)*, 3 (4):3019–3026, 2018. 2

[12] Jonas Frey, David Hoeller, Shehryar Khattak, and Marco Hutter. Locomotion policy guided traversability learning using volumetric representations of complex environments. In *2022 IEEE/RSJ International Conference on Intelligent Robots and Systems (IROS)*, pages 5722–5729. IEEE, 2022. 2, 3, 5

[13] Junzhe He, Chong Zhang, Fabian Jenelten, Ruben Grandia, Moritz Bächer, and Marco Hutter. Attention-based map encoding for learning generalized legged locomotion. *Science Robotics*, 10(105):eadv3604, 2025. 2

[14] Tairan He, Chong Zhang, Wenli Xiao, Guanqi He, Changliu Liu, and Guanya Shi. Agile but safe: Learning collision-free high-speed legged locomotion. *arXiv preprint arXiv:2401.17583*, 2024. 3

[15] David Hoeller, Nikita Rudin, Dhionis Sako, and Marco Hutter. Anymal parkour: Learning agile navigation for quadrupedal robots. *Science Robotics*, 9(88):eadi7566, 2024. 3

[16] Armin Hornung, Kai M. Wurm, Maren Bennewitz, Cyrill Stachniss, and Wolfram Burgard. OctoMap: An efficient probabilistic 3D mapping framework based on octrees. *Autonomous Robots*, 2013. Software available at https://octomap.github.io. 7, 1

[17] Physical Intelligence, Kevin Black, Noah Brown, James Darpinian, Karan Dhabalia, Danny Driess, Adnan Esmail, Michael Equi, Chelsea Finn, Niccolo Fusai, et al. π0. 5: a vision-language-action model with open-world generalization, 2025. *URL https://arxiv. org/abs/2504.16054*, 1(2):3. 2

[18] Songbo Li, Shixin Luo, Jun Wu, and Qiuguo Zhu. Move: Multi-skill omnidirectional legged locomotion with limited view in 3d environments. In *2025 IEEE International Conference on Robotics and Automation (ICRA)*, pages 7647–7653. IEEE, 2025. 3

[19] Qiayuan Liao, Takara E Truong, Xiaoyu Huang, Guy Tevet, Koushil Sreenath, and C Karen Liu. Beyondmimic: From motion tracking to versatile humanoid control via guided diffusion. *arXiv preprint arXiv:2508.08241*, 2025. 3

[20] Minghuan Liu, Zixuan Chen, Xuxin Cheng, Yandong Ji, Ri-Zhao Qiu, Ruihan Yang, and Xiaolong Wang. Visual whole-body control for legged loco-manipulation. *arXiv preprint arXiv:2403.16967*, 2024. 3

[21] Junfeng Long, Junli Ren, Moji Shi, Zirui Wang, Tao Huang, Ping Luo, and Jiangmiao Pang. Learning humanoid locomotion with perceptive internal model. In *2025 IEEE International Conference on Robotics and Automation (ICRA)*, pages 9997–10003. IEEE, 2025. 2, 8

[22] Antonio Loquercio, Ashish Kumar, and Jitendra Malik. Learning visual locomotion with cross-modal supervision. In *IEEE International Conference on Robotics and Automation (ICRA)*, pages 7295–7302. IEEE, 2023. 3

[23] Zhengyi Luo, Ye Yuan, Tingwu Wang, Chenran Li, Sirui Chen, Fernando Castañeda, Zi-Ang Cao, Jiefeng Li, David Minor, Qingwei Ben, et al. Sonic: Supersizing motion tracking for natural humanoid whole-body control. *arXiv preprint arXiv:2511.07820*, 2025. 2

[24] Miles Macklin. Warp: A high-performance python framework for gpu simulation and graphics. https://github.com/nvidia/warp, 2022. NVIDIA GPU Technology Conference (GTC). 3

[25] Daniel Maturana and Sebastian Scherer. Voxnet: A 3d convolutional neural network for real-time object recognition. In *2015 IEEE/RSJ international conference on intelligent robots and systems (IROS)*, pages 922–928. Ieee, 2015. 2

[26] Takahiro Miki, Lorenz Wellhausen, Ruben Grandia, Fabian Jenelten, Timon Homberger, and Marco Hutter. Elevation mapping for locomotion and navigation using gpu. In *2022 IEEE/RSJ International Conference on Intelligent Robots and Systems (IROS)*, pages 2273–2280. IEEE, 2022. 2

[27] Shun Niijima, Ryoichi Tsuzaki, Noriaki Takasugi, and Masaya Kinoshita. Real-time multi-plane segmentation based on gpu accelerated high-resolution 3d voxel mapping for legged robot locomotion. *arXiv preprint arXiv:2510.01592*, 2025. 3

[28] NVIDIA. Isaac Sim. 5

[29] Ri-Zhao Qiu, Yuchen Song, Xuanbin Peng, Sai Aneesh Suryadevara, Ge Yang, Minghuan Liu, Mazeyu Ji, Chengzhe Jia, Ruihan Yang, Xueyan Zou, et al. Wildlma: Long horizon loco-manipulation in the wild. In *2025 IEEE International Conference on Robotics and Automation (ICRA)*, pages 10011–10019. IEEE, 2025. 3

[30] Junli Ren, Tao Huang, Huayi Wang, Zirui Wang, Qingwei Ben, Junfeng Long, Yanchao Yang, Jiangmiao Pang, and Ping Luo. Vb-com: Learning vision-blind composite humanoid locomotion against deficient perception. *arXiv preprint arXiv:2502.14814*, 2025. 2, 3

[31] Nikita Rudin, David Hoeller, Marko Bjelonic, and Marco Hutter. Advanced skills by learning locomotion and local navigation end-to-end. In *2022 IEEE/RSJ International Conference on Intelligent Robots and Systems (IROS)*, pages 2497–2503. IEEE, 2022. 2, 3

[32] John Schulman, Filip Wolski, Prafulla Dhariwal, Alec Radford, and Oleg Klimov. Proximal policy optimization algorithms. *arXiv preprint arXiv:1707.06347*, 2017. 3

[33] Hao Shi, Ze Wang, Shangwei Guo, Mengfei Duan, Song Wang, Teng Chen, Kailun Yang, Lin Wang, and Kaiwei Wang. Oneocc: Semantic occupancy prediction for legged robots with a single panoramic camera. *arXiv preprint arXiv:2511.03571*, 2025. 3

[34] Jingkai Sun, Gang Han, Pihai Sun, Wen Zhao, Jiahang Cao, Jiaxu Wang, Yijie Guo, and Qiang Zhang. Dpl: Depth-only perceptive humanoid locomotion via realistic depth synthesis and cross-attention terrain reconstruction. *arXiv preprint arXiv:2510.07152*, 2025. 2, 3

[35] Wandong Sun, Baoshi Cao, Long Chen, Yongbo Su, Yang Liu, Zongwu Xie, and Hong Liu. Learning perceptive humanoid locomotion over challenging terrain. *arXiv preprint arXiv:2503.00692*, 2025. 2

[36] Generalist AI Team. Gen-0: Embodied foundation models that scale with physical interaction. *Generalist AI Blog*, 2025. https://generalistai.com/blog/preview-uqlxvb-bb.html. 2

[37] Du Tran, Lubomir Bourdev, Rob Fergus, Lorenzo Torresani, and Manohar Paluri. Learning spatiotemporal features with 3d convolutional networks. In *Proceedings of the IEEE international conference on computer vision*, pages 4489–4497, 2015. 2

[38] Huayi Wang, Zirui Wang, Junli Ren, Qingwei Ben, Tao Huang, Weinan Zhang, and Jiangmiao Pang. Beamdojo: Learning agile humanoid locomotion on sparse footholds. *arXiv preprint arXiv:2502.10363*, 2025. 2, 5

[39] Zifan Wang, Teli Ma, Yufei Jia, Xun Yang, Jiaming Zhou, Wenlong Ouyang, Qiang Zhang, and Junwei Liang. Omni-perception: Omnidirectional collision avoidance for legged locomotion in dynamic environments. *arXiv preprint arXiv:2505.19214*, 2025. 2, 3

[40] Meng Wei, Chenyang Wan, Xiqian Yu, Tai Wang, Yuqiang Yang, Xiaohan Mao, Chenming Zhu, Wenzhe Cai, Hanqing Wang, Yilun Chen, et al. Streamvln: Streaming vision-and-language navigation via slowfast context modeling. *arXiv preprint arXiv:2507.05240*, 2025. 3

[41] Botian Xu, Haoyang Weng, Qingzhou Lu, Yang Gao, and Huazhe Xu. Facet: Force-adaptive control via impedance reference tracking for legged robots. *arXiv preprint arXiv:2505.06883*, 2025. 1

[42] Wei Xu and Fu Zhang. Fast-lio: A fast, robust lidar-inertial odometry package by tightly-coupled iterated kalman filter. *IEEE Robotics and Automation Letters*, 6(2):3317–3324, 2021. 5

[43] Wei Xu, Yixi Cai, Dongjiao He, Jiarong Lin, and Fu Zhang. Fast-lio2: Fast direct lidar-inertial odometry. *IEEE Transactions on Robotics*, 38(4):2053–2073, 2022. 5

[44] Ruihan Yang, Minghao Zhang, Nicklas Hansen, Huazhe Xu, and Xiaolong Wang. Learning vision-guided quadrupedal locomotion end-to-end with cross-modal transformers. *arXiv preprint arXiv:2107.03996*, 2021. 3

[45] Naoki Yokoyama, Alex Clegg, Joanne Truong, Eric Undersander, Tsung-Yen Yang, Sergio Arnaud, Sehoon Ha, Dhruv Batra, and Akshara Rai. Asc: Adaptive skill coordination for robotic mobile manipulation. *IEEE Robotics and Automation Letters*, 9(1):779–786, 2023. 3

[46] Chong Zhang, Jin Jin, Jonas Frey, Nikita Rudin, Matías Mattamala, Cesar Cadena, and Marco Hutter. Resilient legged local navigation: Learning to traverse with compromised perception end-to-end. In *2024 IEEE International Conference on Robotics and Automation (ICRA)*, pages 34–41. IEEE, 2024. 3

[47] Qiang Zhang, Zhang Zhang, Wei Cui, Jingkai Sun, Jiahang Cao, Yijie Guo, Gang Han, Wen Zhao, Jiaxu Wang, Chenghao Sun, et al. Humanoidpano: Hybrid spherical panoramic-lidar cross-modal perception for humanoid robots. *arXiv preprint arXiv:2503.09010*, 2025. 3

[48] Ziwen Zhuang, Zipeng Fu, Jianren Wang, Christopher Atkeson, Soeren Schwertfeger, Chelsea Finn, and Hang Zhao. Robot parkour learning. *arXiv preprint arXiv:2309.05665*, 2023. 3

[49] Ziwen Zhuang, Shenzhe Yao, and Hang Zhao. Humanoid parkour learning. *arXiv preprint arXiv:2406.10759*, 2024. 2, 3

Gallant: Voxel Grid-based Humanoid Locomotion and Local-navigation across 3D Constrained Terrains

Supplementary Material

1. Real-world deployment Details

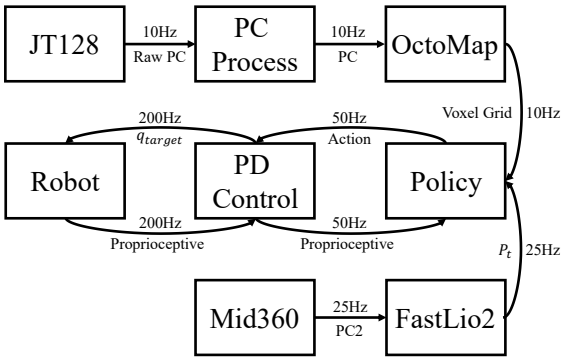

Figure 8. Diagram of information communication.

Target Position Command We use a Unitree G1 robot equipped with a Livox Mid360 LiDAR mounted on its head to run FastLIO2. The Mid360 is installed in a downward-facing orientation and provides a field of view of 360° horizontally and from $-7°$ to $52°$ vertically. The system provides the robot's position in the world coordinate frame at a frequency of 25 Hz. To match this in simulation, the observation frequency of P_t during training is also set to 25 Hz. To align with our training setup, we initialize the robot's starting position at $(0, 0)$ and set the goal position for each run to $(4, 0)$. At each time step, FastLIO2 outputs the current position of the robot (x, y), and the observation relative to the goal is defined as: $P_t = (4, 0) - (x, y) = (4-x, -y)$.

Voxel Grid Processing We use two Hesai JT128 LiDARs mounted at the front and rear of the robot to collect raw point cloud data, which are merged and used for voxel grid construction. The JT128 supports 10 Hz and 20 Hz output modes; empirical testing showed that 20 Hz leads to lower point cloud quality and reduced policy success rates. Therefore, we adopt the more reliable 10 Hz mode and align the simulation accordingly. Each JT128 provides a vertical field of view of approximately 95°, a full 360° horizontal view, and 128 channels. The dual-sensor setup ensures near-complete coverage around the robot. To improve voxel grid quality, the raw point clouds are processed with the Octomap [16] before being passed to the policy. In practice, using Octomap consistently leads to better performance.

Information Communication Our system is fully deployed on a Unitree G1 robot using only an NVIDIA Orin NX, which has limited communication performance. When using TCP to transmit LiDAR data and LCM for internal robot state sharing, we observed a delay of approximately 200 ms in proprioceptive data transmission, which is unacceptable. Thus, we made the following adjustments:

- LiDAR output is clipped to include only points within the voxel grid used for perception, reducing data size.
- The voxel grid from Octomap and that used for observation share memory to avoid redundant transmission.
- Robot state reading and action command delivery are also implemented via shared memory, bypassing LCM.

These optimizations eliminate nearly all communication induced latency, except for inherent sensor delays. Overall information communication process is shown in Fig. 8.

2. Training Details

Hyperparameter Our training framework is derived from [41], and below is a summary of key PPO hyperparameters used in the training process:

Hyperparameter	Value
Environment number	1024×8
Steps per iteration PPO epochs	4
Minibatches	8
Clip range	0.2
Entropy coefficient	0.003
GAE factor λ	0.95
Discount factor γ	0.99
Learning rate	$5e^{-4}$

Table 4. Hyperparameters and their values.

Policy Network Structure The Actor and Critic in our policy share the same network structure but maintain separate parameters. The shared architecture is illustrated in the block diagram below. To be specific, a two-layer MLP with hidden dimensions of 256 is used to encode non-voxel information (e.g., proprioceptive input). Note that the Critic additionally receives privileged observations, resulting in a slightly higher input dimension. This produces an intermediate feature h_{mlp}. In parallel, a three-layer 2D CNN processes the voxel grid input, producing a feature vector h_{cnn}. The two features are concatenated and passed through another MLP to produce a 256-dimensional latent representation. This latent vector is then fed into a final MLP:

- The Actor outputs an action vector of dimension 29.
- The Critic outputs a scalar value estimate.

We use the Mish activation function throughout all layers.

$$
\begin{aligned}
\text{MLP:}\quad & h^{(1)}_{\text{mlp}} = \text{Mish}\big(\text{LN}(W_{\text{mlp},1}x_{\text{mlp}} + b_{\text{mlp},1})\big) \\
& h_{\text{mlp}} = W_{\text{mlp},2}h^{(1)}_{\text{mlp}} + b_{\text{mlp},2}, \quad \dim(h_{\text{mlp}}) = 256 \\
\text{CNN:}\quad & z_1 = \text{Mish}\big(\text{Conv}(x_{\text{cnn}}; C{=}8, k{=}3, s{=}2, p{=}1)\big) \\
& z_2 = \text{Mish}\big(\text{Conv}(z_1; C{=}8, k{=}3, s{=}2, p{=}1)\big) \\
& z_3 = \text{Mish}\big(\text{Conv}(z_2; C{=}8, k{=}3, s{=}2, p{=}1)\big) \\
& h^{\text{flat}}_{\text{cnn}} = \text{Flatten}(z_3) \\
& h^{(1)}_{\text{cnn}} = \text{Mish}\big(\text{LN}(W_{\text{cnn},1}h^{\text{flat}}_{\text{cnn}} + b_{\text{cnn},1})\big) \\
& h_{\text{cnn}} = W_{\text{cnn},2}h^{(1)}_{\text{cnn}} + b_{\text{cnn},2}, \quad \dim(h_{\text{cnn}}) = 64 \\
\text{Fusion:}\quad & f = [h_{\text{mlp}},\, h_{\text{cnn}}] \\
& h^{(1)}_{\text{out}} = \text{Mish}(f) \\
& h_{\text{out}} = \text{Mish}\big(W_{\text{out}}h^{(1)}_{\text{out}} + b_{\text{out}}\big), \quad \dim(h_{\text{out}}) = 256
\end{aligned}
$$

Observation The composition of the observation is detailed in Sec. 3, and the dimensionality of each observation component at a single time step t is summarized in Tab. 5. The dimension of $Height\_Map_t$ shown in Tab. 5 corresponds to its flattened form. Before flattening, it is represented as a 33×33 tensor. Specifically, this map captures the local terrain height around the robot, centered at its base, over a rectangular area with $x \in [-0.8, 0.8]$ m and $y \in [-0.8, 0.8]$ m. A resolution of $0.05m$ is used along both axes, resulting in one height (z) sample per (x, y) grid point. This resolution is consistent with that used in the voxel grid. Instead of applying fixed scaling, the observations are processed using a trainable `vecnorm` module before being fed into the policy. Vecnorm is applied in both training and deployment.

Observation Term	Dimension
P_t	4
$T_{elapse,t}$	1
$T_{left,t}$	1
a_t	29
ω_t	3
g_t	3
q_t	29
$\dot{q}_t$	29
$Voxel\_Grid_t$	$[32 \times 32 \times 40]$
v_t	3
$Height\_Map_t$	1089

Table 5. Observation terms and their dimensions.

Reward Most reward components used in Gallant follow Ben et al. [3], with necessary modifications to support our target-based formulation. In addition to the sparse target-reaching reward r_{reach} introduced in Sec. 3, we incorporate auxiliary shaping terms to improve sample efficiency during early training, as suggested by Rudin et al. [31].

We design the following three general-purpose rewards to encourage effective behavior across a variety of terrain conditions:

- **Directional velocity reward:**

$$r_{\text{velocity\_direction}} = \frac{\mathbf{a}(\mathbf{p}, \mathbf{g}) \cdot \mathbf{v}_t}{\|\mathbf{a}(\mathbf{p}, \mathbf{g}) \cdot \mathbf{v}_t\|_2},$$

  where $\mathbf{v}_t$ is the robot's instantaneous velocity and $\mathbf{a}(\mathbf{p}, \mathbf{g})$ is a direction vector incorporating both goal alignment and obstacle avoidance. It is computed as:

$$\mathbf{a}(\mathbf{p}, \mathbf{g}) = \sum_{j \in \mathcal{N}(\mathbf{p}, r)} w_j\, \mathbf{u}_{r,j} + \kappa \sum_{j \in \mathcal{N}(\mathbf{p}, r)} w_j\, \gamma_j\, \mathbf{t}_j,$$

  where $\mathcal{N}(\mathbf{p}, r)$ denotes obstacle points within radius $r = 1$ m from the robot position $\mathbf{p}$; $\mathbf{u}_{r,j}$ is the repulsion unit vector from obstacle j to the robot; $\mathbf{t}_j$ is a tangential unit vector (left/right) around obstacle j;

$$w_j = \frac{\left[\max\left(1 - \frac{\max(d_j - 0.2,\, 0.02)}{0.8},\, 0\right)\right]^2}{\max(d_j - 0.2,\, 0.02)}$$

  is a distance-based weighting factor, and $\gamma_j = \max(\mathbf{g}^\top \mathbf{d}_j,\, 0)$ filters obstacles behind the goal direction. We set $\kappa = 0.8$ to weight the tangential term. This direction computation is only applied to relevant structures such as cylinders in *Forest* and walls in *Door*, and is efficiently parallelized via `warp`.

- **Head height reward:**

$$r_{\text{head\_height}} = \exp\big(-4(H_{\text{head\_est}} - H_{\text{head}})^2\big),$$

  where $H_{\text{head\_est}}$ is computed by shifting the robot 0.45 m forward along the direction to the goal, averaging the terrain height within a 0.5×0.5 m square, and subtracting a 0.1 m offset. This reward encourages the robot to proactively lower its head to pass under overhead obstacles like ceilings.

- **Foot clearance reward:**

$$r_{\text{feet\_clearance}} = \exp\big(-4(H_{\text{feet\_est}} - H_{\text{feet}})^2\big),$$

  where $H_{\text{feet\_est}}$ is calculated similarly by querying terrain 0.5 m ahead of each foot and averaging the height in a square region. Unlike Ben et al. [3], who use terrain height directly under the foot, our design promotes proactive leg lifting over steps or platforms.

All three rewards are geometry-aware and general-purpose. They are computed consistently across all terrains without task-specific tuning and significantly improve the robot's ability to traverse diverse obstacle configurations.

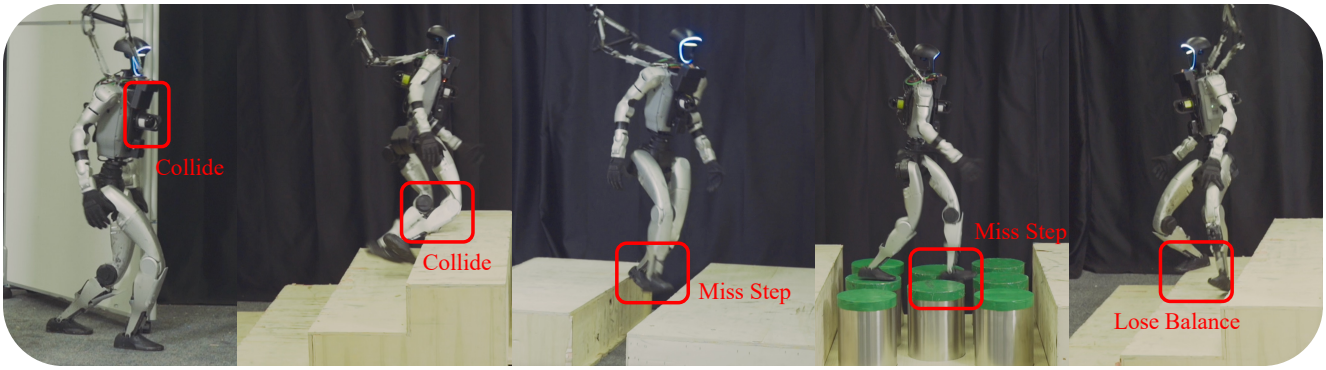

Figure 9. Failure Mode of policy trained by Gallant without LiDAR-related domain randomization.

Domain Randomization In addition to the LiDAR-specific domain randomization described in Sec. 3.2, we apply several general randomization strategies during training to improve policy robustness:

- **Mass randomization:** The masses of the pelvis and torso links are randomized as $m_{\text{rand}} = m \times \mathbf{U}(0.8, 1.2)$, where $\mathbf{U}$ denotes a uniform distribution.
- **Foot-ground contact randomization:** While the ground friction coefficient is fixed at 1.0, the foot joint friction is sampled from $\mathbf{U}(0.5, 2.0)$, and the restitution coefficient from $\mathbf{U}(0.05, 0.4)$.
- **Control parameter randomization:** The joint stiffness and damping parameters are randomized as $K_{p,\text{rand}} = K_p \times \mathbf{U}(0.8, 1.2), K_{d,\text{rand}} = K_d \times \mathbf{U}(0.8, 1.2)$, where K_p and K_d follow the settings in Liao et al. [19].
- **Torso center-of-mass offset:** The center of mass position of the torso is perturbed by an offset sampled from $\mathbf{U}(-0.05, 0.05)$ along each axis.
- **Init Joint Position offset:** A random offset sampled from $\mathbf{U}(-0.1, 0.1)$ is also added to the robot's default joint positions and default joint velocities (0 rad/s). This perturbation is applied during environment reset to randomize the robot's initial state.

Termination We apply several termination conditions during training to encourage effective and safe behavior:

- **Force contact:** If any external force acting on the torso, hip, or knee joints exceeds 100 N at any timestep, the episode is terminated.
- **Pillar fall:** For pillar-based terrains, if a foot penetrates more than 10 cm below the ground level, the episode is terminated to prevent the robot from bypassing the obstacle by jumping off.
- **No movement:** To prevent the agent from exploiting reward shaping by staying on intermediate platforms, the episode is terminated if the robot fails to move at least 1 m away from its initial position within 4 seconds.
- **Fall over:** The episode terminates when the robot loses balance and falls.
- **Feet too close:** Since self-collision is disabled during training to speed up simulation, this condition prevents the robot's feet from crossing or overlapping unnaturally.

Symmetry Following Ben et al. [3], we apply symmetry-based data augmentation to accelerate training. In addition to flipping the proprioceptive observations as in their method, we also apply a flip along the y-axis to the perception representation. Specifically, the $(32, 32, 40)$ grid map is mirrored along the y dimension to align with the flipped proprioceptive input, forming a consistent flipped observation. The reward remains unchanged under the transformation. Both original and flipped samples are stored together in the rollout buffer and jointly used during training.

3. Failure Mode

In Fig. 9, we illustrate typical failure cases of the NoDR variant (Gallant without domain randomization), as discussed in Sec. 4.3.2. These failures fall into three main categories as listed below:

- **Latency-induced collision:** Due to sensor latency, the robot perceives a voxel grid that reflects the environment state from 100–200 ms earlier. Since the policy is trained in simulation with instantaneous observations, it fails to react proactively and collides with obstacles it believes to be farther away.
- **Missed gap detection:** The robot occasionally fails to detect gaps in time, resulting in missed steps. This issue is particularly pronounced in scenarios like the *Platform* task, where long-range gap perception is essential, leading to a lower success rate for NoDR.
- **Poor state estimation:** The robot exhibits imprecise estimation of its own body state. While it may avoid collisions or missed steps on stairs, it still enters unstable configurations and loses balance.

These observations highlight the importance of domain randomization, especially in simulating LiDAR latency and noise. Without such randomization, the policy fails to generalize effectively to real-world deployments.